Inorganic Chemistry

ARTICLE

pubs.acs.org/IC

Iron Silylamide-Grafted Periodic Mesoporous Silica

Thomas Deschner,[†] Karl W. Törnroos,[†] and Reiner Anwander*[,‡]

[†]Department of Chemistry, University of Bergen, Allégaten 41, N-5007 Bergen, Norway

[‡]Institut für Anorganische Chemie, Eberhard Karls Universität Tübingen, Auf der Morgenstelle 18, D-72076 Tübingen, Germany

Supporting Information

ABSTRACT: The surface chemistry of a series of well-defined metalorganic ferrous and ferric iron complexes on periodic mesoporous silica (PMS) was investigated. In addition to literature known $Fe^{II}[N(SiMe_3)_2]_2(THF)$, $Fe^{II}[N(SiPh_2Me_2)_2]_2$, and $Fe^{III}[N(SiMe_3)_2]_2Cl(THF)$, the new complexes $[Fe^{II}\{N(SiHMe_2)_2\}_2]_2$ and $Fe^{III}[N(SiHMe_2)_2]_3(\mu\text{-}Cl)Li(THF)_3$ were employed as grafting precursors. Selection criteria for the molecular precursors were the molecular size (monoiron versus diiron species), the oxidation state of the iron center (II versus III), and the functionality of the silylamido ligand (e.g., built-in spectroscopic probes). Hexagonal channel-like MCM-41 and cubic cage-like SBA-1 were chosen as two distinct PMS materials. The highest iron load (12.8 wt %) was obtained for hybrid material $[Fe^{II}\{N(SiHMe_2)_2\}_2]_2$@MCM-41 upon stirring the reaction mixture iron silylamide/PMS/*n*-hexane for 18 h at ambient temperature. Size-selective grafting and concomitantly extensive surface silylation were found to be prominent for cage-like SBA-1. Here, the surface metalation is governed by the type of iron precursor, the pore size, the reaction time, and the solvent. The formation of surface-attached iron−ligand species is discussed on the basis of diffuse reflectance infrared Fourier transform (DRIFT) and electron paramagnetic resonance (EPR) spectroscopy, nitrogen physisorption, and elemental analysis.

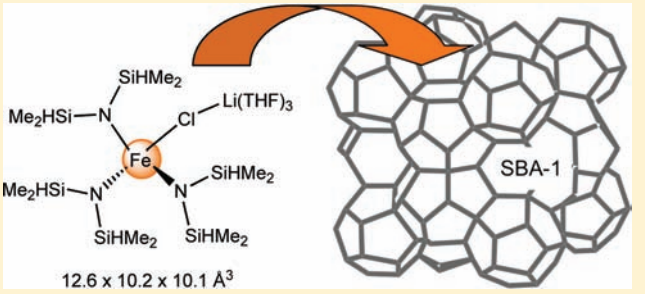

INTRODUCTION

Iron-promoted chemical transformations are currently intensively studied in the field of sustainable metalorganic catalysis.[1−4] While iron initiators for the polymerization of olefins (post-metallocene catalysts) have been successfully investigated since 1998,[5,6] the past five years have witnessed a formidable development of efficient and selective iron-based catalysts for organic synthesis, for example, cross-coupling reactions.[7−14] These recent achievements in homogeneous iron catalysis seem to be long overdue given the importance of heterogeneous iron catalysis (e.g., Haber−Bosch process)[15] and the omnipresence of iron in biological systems.[16−18] Abundant, mostly nontoxic, and redox-active iron is the key element in metalloproteins, which transport and metabolize small molecules (dioxygen, dinitrogen, methane, etc.) as well as mediate electron-transfer reactions.[16−23] Although the design of biomimetic and bioinspired iron catalysts is obvious,[24] there are only a few reports on the variation of well-defined catalytic iron centers via immobilization techniques such as tethering[25−27] or grafting of iron complexes onto the surface of nanoporous oxidic host materials.[28−34] Whereas readily available ferrocene and iron carbonyl derivatives have been routinely employed for performing intrazeolite chemistry,[33,35−38] until now only iron siloxide complexes have been used for the post-functionalizing of periodic mesoporous silica (PMS).[28,29] Single-site Fe(III) and diiron species were generated on the surface of SBA-15 by using $Fe^{III}[OSi(OtBu)_3]_3(Do)$ (Do = THF, OEt_2) and $[Fe^{II}\{OSi(OtBu)_3\}_2]_2$, $[(tBuO)_3SiO]_3Fe^{III}(NMe_2C_2H_4NMe_2)Fe^{III}[OSi(OtBu)_3]_3$ as well as $[NEt_4]_2[\{(tBuO)_3SiO\}_3Fe^{III}OFe^{III}\{OSi(OtBu)_3\}_3]$ as molecular precursors and the resulting hybrid materials exploited for the catalytic oxidation of alkanes, alkenes, and arenes.[28,29] Furthermore, ferrous alkyl complex $LFe^{II}(CH_2SiMe_3)_2$ (L = 2,3-dimethyl-1,4-[2′,6′-diisopropylphenyl]-*N*,*N*′-diazadiene) and aryl complexes $Fe^{II}(C_6H_2tBu_3\text{-}2,4,6)_2$ as well as $[Fe^{II}(C_6H_2Me_3\text{-}2,4,6)(\mu\text{-}C_6H_2Me_3\text{-}2,4,6)]_2$ were employed to study the implications of nuclearity for the grafting onto silica, silica−alumina, and alumina supports.[30,31] The latter metalorganic hybrid materials and Fe(TPP)Cl@MCM-41 (TPP = tetraphenylporphyrin)[32] were used for cyclohexene oxidation. Nonetheless, iron incorporation either during hydrothermal synthesis[39−44] or via incipient wetness impregnation[32,45−48] have been the predominant reaction protocols to access such nanostructured catalysts, whereas microporous FeZSM-5 has been the lead catalyst because of its high activity for the reduction of nitrogen oxides[49] and for the selective oxidation of hydrocarbons with nitrous oxide as the oxidant.[50,51]

We have been developing the grafting of metal (silyl)amide complexes onto PMS[52] as a mild variant of SOMC (surface organometallic chemistry).[53−55] Assuming a pK_a value of around 5−7 (similar to silica gel) for the silanol groups of PMS materials, metal silylamides display ideal nondestructive surface reactivity.[56,57] The mild reaction conditions of such heterogeneously performed

Received: April 18, 2011
Published: July 01, 2011

silylamine elimination protocols give access to (a) thermodynamically stable metal siloxide bonds (oxophilic metal centers), (b) a unique hydrophobic platform because of concomitant surface silylation, (c) favorable atom economy, (d) monometallic/low-nuclear surface metal−ligand moieties because of the steric bulk of remaining silylamido ligands, (e) tailor-made silylamido ligands decorated with spectroscopic probes (e.g., "Si−H"), (f) low-coordinated/donor-free and hence reactive surface metal−ligand moieties because of the release of weakly coordinating and hence easily separable silylamines, (g) pure/salt-free hybrid materials because of the absence of any insoluble byproducts, and finally (h) consecutive metal functionalization via silylamido ligand exchange. Moreover, such thermally robust silylamido ligands provide a stabilizing environment for most of the main group and transition metals in distinct oxidation states.[58−61] It should be also noted that the "silylamide route" is a most prominent method, especially in rare-earth metal chemistry, for the high-yield synthesis of pure catalyst precursors for polymerization and carbon−heteroelement bond forming reactions (e.g., hydroamination).[52,62] Not surprisingly, the heterogeneously performed variant has been initially reported for lanthanide elements but recently exploited for main group and d-transition metal elements as well.[63,64] On the other hand, cage-like PMS materials like for example SBA-1,[65,66] SBA-2,[65,66] SBA-6,[67] SBA-16[65,66] or KIT-5[68] feature a unique pore topology consisting of large supercages interconnected by smaller pores, qualifying the envisaged functionalized materials for size-selective reactions. Concomitantly, the pore curvature might provide a confinement of the catalytically active species comparable to the active site in enzymes.[52,69]

Our present work reports on the SOMC of mono- and binuclear iron(II)/(III) silylamide complexes on PMS materials. The main emphasis was put on the use of PMS materials with different pore configuration/size (channel-like hexagonal MCM-41 versus cage-like cubic SBA-1) as well as the use of iron complexes bearing tailor-made silylamido ligands. Accordingly, not only literature known $Fe^{II}[N(SiMe_3)_2]_2(THF)$,[70] $Fe^{II}[N(SiPh_2Me_2)_2]_2$,[71] and $Fe^{III}[N(SiMe_3)_2]_2Cl(THF)$[72] were employed as molecular precursors but also new $[Fe^{II}\{N(SiHMe_2)_2\}_2]_2$ and $Fe^{III}[N(SiHMe_2)_2]_3(\mu\text{-}Cl)Li(THF)_3$ derived from a sterically less demanding probe ligand.

RESULTS AND DISCUSSION

Choice of PMS Support Materials and Iron Silylamide Precursors. Hexagonal MCM-41 (space group *p6mm*) and cubic SBA-1 (*Pm*3*n*) were selected to study any distinct grafting behavior of the iron silylamide complexes associated with a channel- or a cage-like pore configuration. Samples of pore-enlarged MCM-41 (**1** and **2**; $d_{p,ads.}$ = 4.0 nm)[73] and standard SBA-1 (**3** and **5**; D_{me} = 4.5 nm)[74−76] were synthesized according to recent literature procedures. The method described by Vinu et al.[77] was employed to generate the pore-enlarged SBA-1 material **4**. Utilizing a prolonged hydrothermal treatment of the SBA-1 synthesis gel (6 h instead of 1 h at 100 °C) afforded a considerable expansion of the pore system in PMS **4** as derived from nitrogen physisorption data and a shift of the relative intensities of the (200) and (211) reflections to lower angles (for powder XRD patterns, see Supporting Information). Given that the pore diameter d_p of the selected MCM-41 is about 20 Å wider than the molecular dimensions of the iron precursors (vide infra), the silylamide grafting should be less affected by any molecular diffusion effects through the cylindrical mesopores or even pore blockage. On the other hand, it has been shown that the intrinsic A_3B cage structure of SBA-1, featuring small interconnecting windows, is prone to size-selective immobilization reactions and intrapore chemistry.[63,78−80] On the basis of electron diffraction experiments, Sakamoto et al.[67] proposed that two A cages are interconnected by windows of approximate size 15 × 22 Å and rather small windows of around 2 Å in diameter between A and B cages. Moreover, Anderson et al. concluded from calculations that all window diameters are smaller than 13 Å.[81] Alternatively, the accessibility of the SBA-1 pore system and a rough estimation of the pore openings might be obtained via grafting of silylating reagents of similar size.[82] Also in the case of SBA-1 **4**, expansion of the pore system by hydrothermal post-treatment might counteract possible pore blockage effects via predominant functionalization of the pore openings.[63]

Having in mind the benefits of the heterogeneously performed silylamide route, we decided to investigate for the first time the immobilization behavior of iron silylamide complexes.[83−86] Selection criteria for the iron precursors were (a) the molecular size, that is, smaller than the theoretically derived pore openings of unmodified SBA-1 **3** and **5** synthesized by standard procedures, (b) the oxidation state of the iron metal center (II versus III), and (c) the silylamido ligand functionality (Figure 1, Scheme 1).

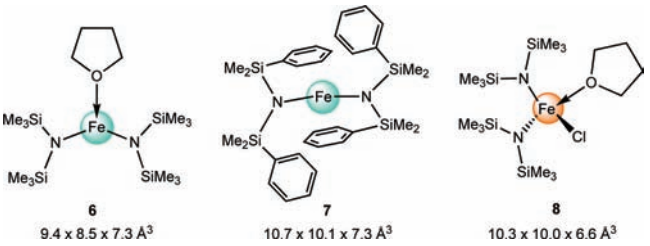

Figure 1. Iron silylamide precursors under study (approximate van der Waals dimensions from crystallographic data are indicated; see also Supporting Information).[70−72]

Scheme 1. Synthesis of Ferrous and Ferric Iron Bis(dimethylsilylamide) Complexes[a]

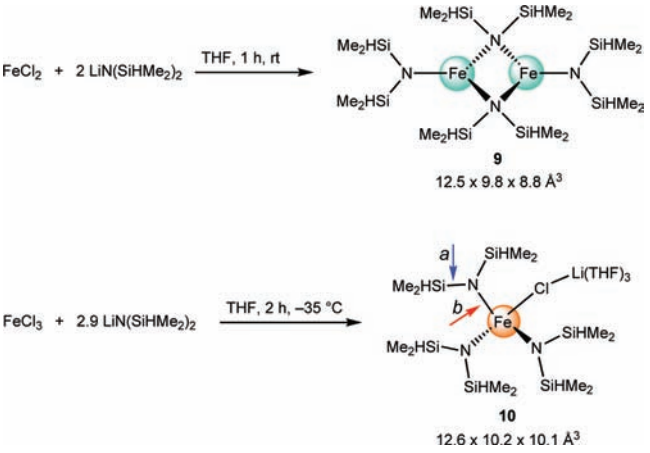

[a] Bonds prone to protonolysis reactions are indicated by arrows a and b; approximate van der Waals dimensions from crystallographic data are listed; see also Supporting Information.

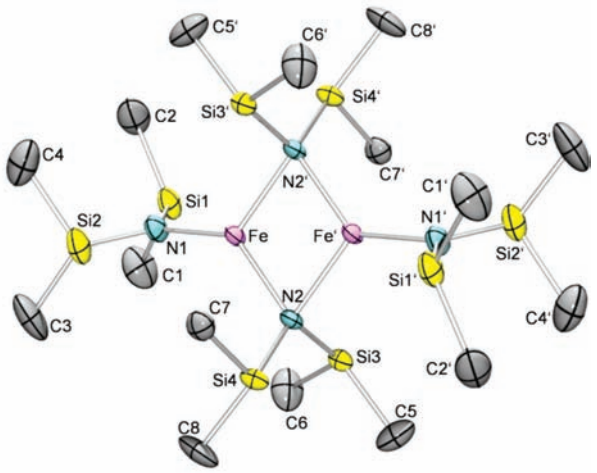

Figure 2. Molecular structure of compound $[Fe^{II}\{N(SiHMe_2)_2\}_2]_2$ (**9**) with 50% probability ellipsoids; hydrogen atoms are omitted for clarity. Selected bond lengths/distances [Å] and angles [deg]: Fe−N1 1.903(2), Fe−N2 2.017(2), Fe---Fe 2.6733(6); N1−Fe−N2 134.96(7), Fe−N2−Fe′ 82.18(6), Si1−N1−Si2 126.5(1), Fe−N1−Si1 116.8(1), Fe−N1−Si2 116.7(1), Fe−N2−Si3 111.57(9), Fe−N2−Si4 118.93(9).

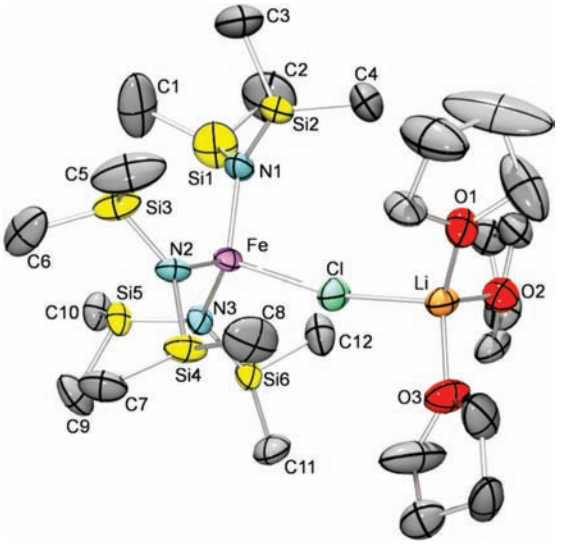

Figure 3. Molecular structure of compound $Fe^{III}[N(SiHMe_2)_2]_3(\mu\text{-}Cl)Li(THF)_3$ (**10**) with 50% probability ellipsoids; hydrogen atoms are omitted for clarity. Selected bond lengths [Å] and angles [deg]: Fe−N1 1.926(4), Fe−N2 1.943(4), Fe−N3 1.919(4), Fe−Cl1 2.322(2); N1−Fe−N2 115.2(2), N1−Fe−N3 112.5(2), N2−Fe−N3 111.2(2), N1−Fe−Cl1 103.9(1), N2−Fe−Cl1 106.0(1), N3−Fe−Cl1 107.2(1), Si1−N1−Si2 123.0(3), Si3−N2−Si4 123.3(2), Si5−N3−Si6 121.7(2), Fe−N1−Si1 121.3(3), Fe−N1−Si2 115.7(3), Fe−N2−Si3 121.2(2), Fe−N2−Si4 115.4(2), Fe−N3−Si5 113.7(2), Fe−N3−Si6 124.2(2), Fe−Cl1−Li 163.1(2).

In addition to literature known complexes $Fe^{II}[N(SiMe_3)_2]_2$-(THF) (**6**),[70] $Fe^{II}[N(SiPh_2Me_2)_2]_2$ (**7**),[71] and $Fe^{III}[N(SiMe_3)_2]_2$-Cl(THF) (**8**)[72] carrying thermally very robust silylamido ligands (Figure 1), we tackled the synthesis of new iron silylamide complexes bearing the SiH functionality as an IR-spectroscopic probe. Scheme 1 summarizes the successful syntheses of complexes $[Fe^{II}\{N(SiHMe_2)_2\}_2]_2$ (**9**) and $Fe^{III}[N(SiHMe_2)_2]_3$-$(\mu\text{-}Cl)Li(THF)_3$ (**10**). The syntheses starting out from ferrous and ferric chlorides required optimizing with respect to solvent, reaction temperature, reaction time, and alkali metal precursor. The main challenge of the syntheses utilizing salt metathesis protocols was to control the reductive behavior of the SiH moiety impeding the synthesis of the trivalent bis(dimethylsilyl)amide derivative. Several attempts to synthesize homoleptic $Fe^{III}[N(SiHMe_2)_2]_3$ failed, mainly resulting in the formation of $[Fe^{II}\{N(SiHMe_2)_2\}_2]_2$ (**9**). Nevertheless ate complexation seems to sufficiently stabilize ferric complex **10**.

The solid-state structures of complexes **9** and **10** were crystallographically authenticated by single crystal X-ray diffraction (Figures 2 and 3, Table 3). Like the sterically more demanding $[Fe^{II}\{N(SiMe_3)_2\}_2]_2$[70,87] complex **9** revealed a dimeric structure with bridging amido ligands and donor solvent-free iron centers.

The Fe−N bond distances appear to be slightly shorter than those found for complex $[Fe^{II}\{N(SiMe_3)_2\}_2]_2$ (terminal: 1.923(3) and 1.927(3) Å; bridging: 2.086(2) and 2.083(2) Å), reflecting decreased steric encumbrance at the metal centers. A VT (variable temperature) ^{1}H NMR spectroscopic study conducted in the range between 183 and 313 K (see Supporting Information), evidences a dimeric structure of complex **9** in solution, in accordance with the solid-state structure.

Complex $Fe^{III}[N(SiHMe_2)_2]_3(\mu\text{-}Cl)Li(THF)_3$ (**10**) is a rare example of a metalorganic ferric amide complex.[60,61] The iron(III) center adopts a distorted tetrahedral coordination geometry featuring three silylamido and one $ClLi(THF)_3$ ligand (Figure 3).

Because of enhanced steric crowding of the iron metal center, the Fe−N bond lengths of av. 1.929 Å are slightly elongated compared to those in ferrous complex **9** (terminal: 1.903(2) Å) and in ferric complexes $Fe^{III}[N(SiMe_3)_2]_3$ (Fe−N: 1.918 Å)[88] and $Fe^{III}[N(SiMe_3)_2]_2Cl(THF)$ (**8**: Fe−N_{av}, 1.907 Å; Fe−Cl, 2.2510(7) Å).[72] The Fe−Cl distance in **10** (2.322(2) Å) is comparable to that in $Fe^{II}[N(SiMe_3)_2]_2(\mu\text{-}Cl)Li(THF)_3$ (2.318(2) Å) showing the same μ_2-bridging $ClLi(THF)_3$ ligand.[89] For comparison, the same structural motif was observed for $Nd^{III}[N(SiMe_3)_2]_3$-$(\mu\text{-}Cl)Li(THF)_3$.[90]

Functionalization of MCM-41. Grafting of $[Fe^{II}\{N(SiHMe_2)_2\}_2]_2$ (**9**) onto MCM-41 (**1**, pore diameter $d_{p,ads}$ = 4.0 nm, Brunauer−Emmett−Teller (BET) surface a_s = 1100 m^2/g, pore volume V_p = 1.17 cm^3/g, Table 1, Figure 4) afforded hybrid material **1b** with a drastically reduced pore volume (ΔV_p = 0.85 cm^3/g) and diameter ($\Delta d_{p,ads}$ = 1.7 nm) as well as half the BET surface area (620 m^2/g) (Figure 4). For comparison, surface silylation with 1,1,3,3-tetramethyldisilazane, a standard reaction performed in our laboratory to determine the surface silanol population of siliceous materials,[91] produced material **1a** ($d_{p,ads}$ = 3.1 nm, a_s = 650 m^2/g, V_p = 0.63 cm^3/g, 3.56 mmol SiOH/g Table 1, Figure 4). Even though the BET surface area of materials **1a** and **1b** are equal, the highly decreased pore volume and diameter of ferrous hybrid material **1b** give a strong indication of the grafted species to show a larger dimension than the $SiHMe_2$ moiety.

The IR spectrum of hybrid material **1b** recorded as a Nujol mull revealed only a relatively broad signal for the SiH stretching vibration centered at 2143 cm^{-1} (Figure 5). For comparison hybrid material $SiHMe_2$@MCM-41 (**1a**) and precursor $[Fe^{II}\{N(SiHMe_2)_2\}_2]_2$ (**9**) display sharp resonances at 2153 and 2116/2086 cm^{-1}, respectively.

Calculation of the N/Fe and C/N ratios for material **1b** gave values of 1.0 and 3.8, respectively, which are close to the proposed surface species **A** (Figure 6, N/Fe = 1.00 and C/N = 4). Note that these calculations are only rough estimates not fully satisfying any competing surface silylation and hindered nitrogen analysis in

Table 1. Surface Area, Pore Volume, Pore Diameter, and Analytical Data of Parent and Functionalized MCM-41 Materials

	sample/precursor	a_s[m^2/g][a]	$d_{p,ads}$[nm][b]	V_p[cm^3/g][c]	C [wt %][d]	N [wt %][d]	Fe [wt %][d,e]	N/Fe	C/N
1	MCM-41 (a = 5.48 nm)	1100	4.0	1.17					
1a	$SiHMe_2$@MCM-41	650	3.1	0.63	7.08	0.15			
1b	$[Fe^{II}\{N(SiHMe_2)_2\}_2]_2$@MCM-41	620	2.3	0.32	10.54	3.22	12.8	1.00	3.83
1c	$Fe^{III}[N(SiHMe_2)_2]_3(\mu$-Cl)Li$(THF)_3$@MCM-41	540	2.6	0.42	11.50	1.66	6.2	1.07	8.08
2	MCM-41 (a = 5.58 nm)	1060	4.0	1.14					
2a	$SiHMe_2$@MCM-41	740	3.3	0.73	6.94	<0.1			
2b	$Fe^{II}[N(SiPhMe_2)_2]_2$@MCM-41	430	2.6	0.32	21.89	0.67	9.7	0.27	38.5

[a] Specific BET surface area. [b] Pore diameter according to the maximum of the BJH pore size distribution calculated from the adsorption branch; all samples were pretreated at 250 °C (parent materials), 100 °C (silylated samples), and 25 °C (grafted samples) in vacuo until the pressure was $<10^{-3}$ Torr. [c] Pore volume determined at the relative pressure $p/p_0 = 0.975$. [d] Elemental analysis obtained after treatment at 100/25 °C (silylated/grafted samples) in vacuo ($<10^{-3}$ Torr). [e] Iron content from atom absorption spectroscopy (AAS) of HF treated samples.

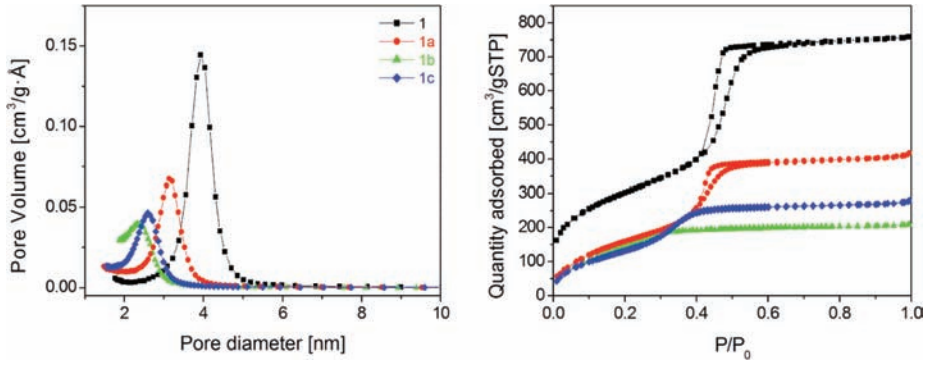

Figure 4. Nitrogen adsorption/desorption isotherms (right) and corresponding BJH pore size distributions (right) of MCM-41 (**1**, black solid squares), $SiHMe_2$@MCM-41 (**1a**, red solid circles), $[Fe^{II}\{N(SiHMe_2)_2\}_2]_2$@MCM-41 (**1b**, green solid triangles), and $Fe^{III}[N(SiHMe_2)_2]_3(\mu$-Cl)Li$(THF)_3$ (**1c**, blue solid diamonds).

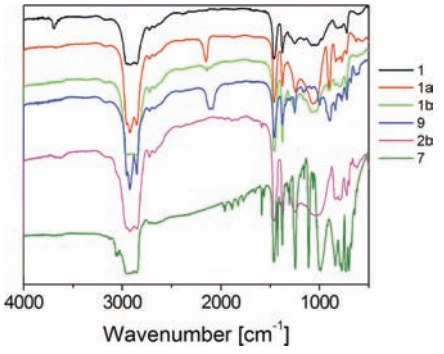

Figure 5. IR spectra (Nujol) of mesoporous silica MCM-41 (**1**) and hybrid materials **1a**, **1b**, and **2b**, and precursors $[Fe^{II}\{N(SiHMe_2)_2\}_2]_2$ (**9**) and $Fe^{II}[N(SiPhMe_2)_2]_2$ (**7**).

the presence of silicon. The observed high iron loading for material **1b** (12.8 wt %) is also consistent with the formation of species like **C** and **D** (Figure 6) while the extensive pore filling and small pore diameter point to the preservation of dinuclear moieties as represented by **C**.

As evidenced by N_2-physisorption, grafting of tailor-made $Fe^{III}[N(SiHMe_2)_2]_3(\mu$-Cl)Li$(THF)_3$ (**10**) onto MCM-41 **1** produced material **1c** with a surface area of 540 m^2/g which is lower than that of ferrous hybrid material **1b**, however, with comparatively higher pore volume and pore size (0.42 cm^3/g, 2.6 nm). Hence the ferric surface species occupy less mesopore space. The diffuse reflectance infrared Fourier transform (DRIFT) spectrum of **1c** shows a broad peak in the Si−H region with two maxima at around 2100 cm^{-1} (surface bound Fe^{III}−$N(SiHMe_2)_2$ moieties; cf., precursor **10**: 2119 cm^{-1}; Figure 7) and 2136 cm^{-1} (surface silyl groups). Intact surface-bonded Fe^{III}−$N(SiHMe_2)_2$ are unequivocally proven by the IR spectrum of **1c** after exposure to moist air showing the released silylamine (cf., Supporting Information). The iron content of hybrid material **1c** was approximately half of that found for **1b** (6.2 vs 12.8 w%). Taking also into account the N/Fe and C/N elemental ratios of 1.07 and 8.08, respectively, the formation of bipodally grafted species **G** and extensive surface silylation (**J**, Figure 6) are suggested. Note that for sterically very crowded silylamide complexes surface silylation can occur via two distinct pathways indicated by arrows **a** and **b** in formula **10** (Scheme 1).[80] Of course, the existence of a certain amount of monopodal ferric surface species **H** cannot be ruled out.

The surface reaction of monomeric ferrous complex $Fe^{II}[N(SiPhMe_2)_2]_2$ on a second sample of MCM-41 (**2**, $d_{p,ads}$ = 4.0 nm, a_s = 1060 m^2/g, V_p = 1.14 cm^3/g, 3.47 mmol SiOH/g, Table 1, Figure 8) yielded hybrid material **2b**. While the pore volume and pore diameter decreased similarly as for $[Fe^{II}\{N(SiHMe_2)_2\}_2]_2$@MCM-41 (**1b**) (72 and 32%, respectively, compared to the parent material), an even higher drop of the BET surface area to 430 m^2/g was observed. The IR spectrum of **2b** revealed unreacted silanol groups and silanols interacting with the π-system of the phenyl substituents (broad peak at 3622 cm^{-1}, Figure 5).[91,92] The carbon content of hybrid material **2b** was significantly higher than in **1b** reflecting the higher carbon

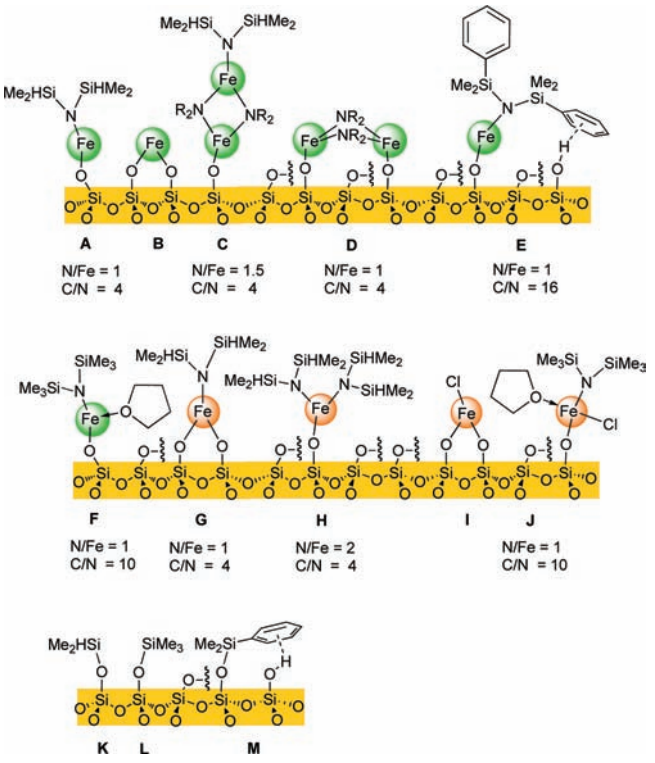

Figure 6. Possible surface species of iron hybrid materials under study. LiCl is omitted for species **G** and **H**.

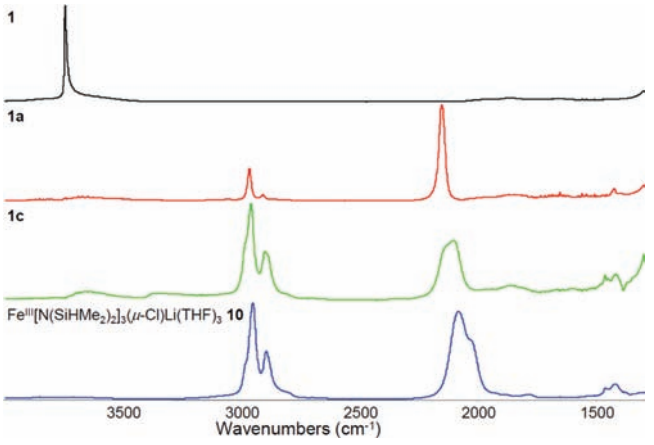

Figure 7. IR spectra (DRIFT) of mesoporous silica MCM-41 (**1**), hybrid materials **1a** and **1c** as well as precursor $Fe^{III}[N(SiHMe_2)_2]_3(\mu\text{-}Cl)Li(THF)_3$ (**10**) in the range of 1300−4000 cm^{-1} (for the range of 400−4000 cm^{-1}, see Supporting Information).

content of the employed precursor. The high iron content of 9.7 wt % combined with N/Fe and C/N ratios of 0.27 and 38.5 are remarkable, suggesting bipodally grafted iron centers (**B**) and bulky $\equiv SiOSiPhMe_2$ groups (**M**) as the predominant surface species, along with monopodal **E** as a minor component (Figure 6).

Functionalization of SBA-1. Initially, we investigated the grafting of solvent-free ferrous complex $[Fe^{II}\{N(SiHMe_2)_2\}_2]_2$ (**9**) onto cage-like SBA-1 (**3**, D_{me} = 4.5 nm, a_s = 1390 m^2/g, V_p = 0.88 cm^3/g, 3.73 mmol SiOH/g Table 2, Figure 9) in hexane as a solvent.

The IR spectrum of material **3b**, obtained by using a reaction period of 18 h, clearly revealed that the silanol groups were only partially functionalized. Further, the pore volume, BET surface area, and pore diameter of hybrid material $[Fe^{II}\{N(SiHMe_2)_2\}_2]_2$@SBA-1 (**3b**) were in the same region as found for the silylated material $SiHMe_2$@SBA-1 (**3a**). Taking into account the rather low iron content of 2.3 wt %, only metalation at the outer domains of the SBA-1 particles is suggested, as reported previously for the respective magnesium hybrid material $[Mg\{N(SiHMe_2)_2\}_2]_2$@SBA-1.[63] While an N/Fe ratio of 0.98 proposes that each iron center has one silylamido ligand attached to it, the high C/N ratio of 13.5 clearly indicates a high degree of surface silylation. A reasonable scenario would be that diiron surface species such as **D** block the windows so that diffusion of the bulky dimeric iron precursor **9** is slowed down considerably. In contrast the released sterically less demanding bis(dimethylsilyl)amine can enter the cages to produce surface sites of type **K**.

Effect of the Solvent. To further study this size effect we conducted the surface reaction in THF affording material $[Fe^{II}\{N(SiHMe_2)_2\}_2]_2$@SBA-1(THF) (**3c**). It has been shown by Power et al. that the corresponding binuclear bis(trimethylsilyl)amide complex $[Fe^{II}\{N(SiMe_3)_2\}_2]_2$ forms the less sterically demanding monomeric adduct $Fe^{II}[N(SiMe_3)_2]_2(THF)$ in THF.[70] Although the use of THF as a solvent gave a higher iron load (3.3 wt %), the IR spectrum of **3c** showed a high degree of unreacted silanol groups (Figure 10). Moreover, a very low nitrogen content (N/Fe <0.5) and a high C/N ratio of 36.1 indicate bipodally grafted iron species **B**(THF) to be prevalent as well as a much higher degree of surface silylation compared to **3b**. The high C/N ratio for material **3c** can certainly be affected by the presence of coordinated and/or occluded THF molecules. Using toluene as a solvent, hybrid material $[Fe^{II}\{N(SiHMe_2)_2\}_2]_2$@SBA-1(toluene) (**3d**) was obtained with similar surface area, pore volume/diameter, and iron content as **3b** (Table 2, Figures 9 and 10). Exclusively bipodally grafted iron centers **B** are proposed by elemental analysis (N < 0.1%). Noteworthy, all ferrous hybrid materials **3b**−**3d** revealed a considerable amount of unreacted silanol groups and an intense Si−H stretching vibration at 2151 cm^{-1} (species **K**) (Figure 10).

Effect of the Reaction Time. To further investigate any diffusion effects, complex $[Fe^{II}\{N(SiHMe_2)_2\}_2]_2$ (**9**) was allowed to react for four days with SBA-1 **3** in hexane as a solvent. The resulting hybrid material **3e** displayed a considerably lower BET surface area, pore diameter, and pore volume than materials **3b**−**d** (Table 2, Figure 9). Moreover, a completely functionalized surface is corroborated by the absence of free silanol groups (Figure 11), and increased amounts of C, N, and Fe (9.67, 1.45, and 4.3 wt %, respectively). N/Fe and C/N ratios of 1.22 and 7.8 are in accordance with a mixture of surface species as represented by **A**, **C**, and **D**, and some degree of surface silylation (species **K**), respectively. The presence of $[Fe{-}N(SiHMe_2)_2]_2$ surface species is illustrated by a low-energy shoulder of the $\equiv SiOSiHMe_2$ band in the DRIFT spectrum of material **3e** (Figure 11). Although entrapment of released silylamine/ammonia inside the cages could be excluded because of the absence of any N−H stretching vibration at around 3380 cm^{-1}, intrapore confinement of unreacted precursor **9** cannot be ruled out completely.

Additionally, it is important to point out that the ferrous and ferric bis(dimethylsilyl)amide complexes slowly decompose over time forming a black oily component which has not been further characterized. The noninnocent bis(dimethylsilyl)amide ligand might engage in reductive degradation processes which are also

dx.doi.org/10.1021/ic200788f |*Inorg. Chem.* 2011, 50, 7217–7228

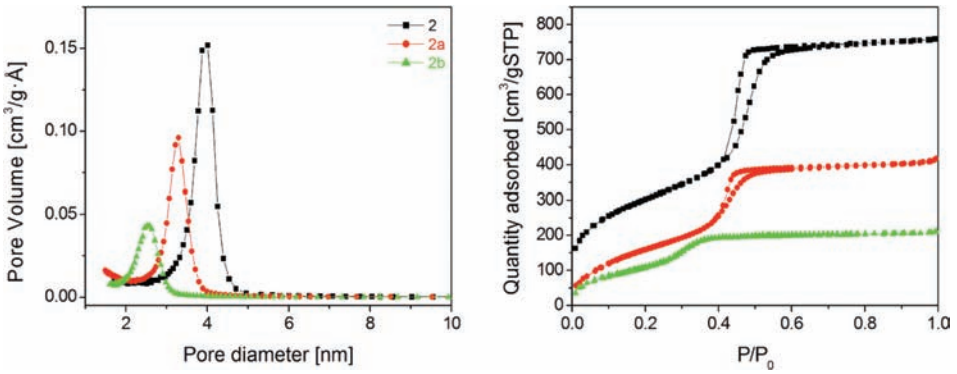

Figure 8. Nitrogen adsorption/desorption isotherms (right) and corresponding BJH pore size distributions (right) of MCM-41 (**2**, black solid squares), $SiHMe_2$@MCM-41 (**2a**, red solid circles), and $Fe^{II}[N(SiPhMe_2)_2]_2$@MCM-41 (**2b**, green solid triangles).

Table 2. Surface Area, Pore Volume, Pore Diameter, and Analytical Data of Parent and Functionalized SBA-1 Materials

	sample/precursor [cell parameter *a*] (solvent)	a_s [m^2/g][a]	D_{me} [nm][b]	V_p [cm^3/g][c]	C [wt %][d]	N [wt %][d]	Fe [wt %][d,e]	N/Fe	C/N
3	SBA-1 [a = 8.29 nm]	1390	4.5	0.88					
3a	$SiHMe_2$@ SBA-1	1040	4.1	0.49	7.36	<0.1			
3b	$[Fe^{II}\{N(SiHMe_2)_2\}_2]_2$@ SBA-1(hexane)	940	4.1	0.46	6.62	0.57	2.3	0.98	13.5
3c	$[Fe^{II}\{N(SiHMe_2)_2\}_2]_2$@ SBA-1(THF)	1000	4.2	0.52	12.08	0.39	3.3	0.47	36.1
3d	$[Fe^{II}\{N(SiHMe_2)_2\}_2]_2$@ SBA-1(toluene)	940	4.1	0.45	7.14	<0.1	2.4	n.d.	n.d.
3e	$[Fe^{II}\{N(SiHMe_2)_2\}_2]_2$@ SBA-1(hexane)[f]	840	3.9	0.37	9.67	1.45	4.7	1.22	7.8
4	SBA-1 [a = 8.61 nm]	1260	4.7	0.88					
4a	$SiHMe_2$@ SBA-1	1000	4.3	0.52	6.92	<0.1			
4b	$[Fe^{II}\{N(SiHMe_2)_2\}_2]_2$@SBA-1	780	4.1	0.37	9.44	1.61	6.1	1.05	6.8
4c	$Fe^{II}[N(SiPhMe_2)_2]_2$@SBA-1	1000	4.4	0.57	10.48	0.34	2.6	0.52	36.0
5	SBA-1 [a = 8.50 nm]	1320	4.5	0.82					
5a	$SiHMe_2$@ SBA-1	1110	4.2	0.51	6.61	0.11			
5b	$Fe^{II}[N(SiMe_3)_2]_2$(THF)@SBA-1	1130	4.3	0.55	6.61	0.35	1.2	1.16	22.0
5c	$Fe^{III}[N(SiHMe_2)_2]_3(\mu\text{-Cl})Li(THF)_3$@SBA-1	990	4.2	0.47	7.02	0.16	0.97	0.66	51.2
5d	$Fe^{III}[N(SiMe_3)_2]_2Cl(THF)$@SBA-1	1100	4.3	0.52	9.33	0.33	3.3	0.40	33.0
5e	$Fe^{II}[N(SiMe_3)_2]_2(THF)$@SBA-1[f]	1050	4.3	0.54	7.65	0.25	1.9	0.61	35.7
5f	$Fe^{III}[N(SiHMe_2)_2]_3(\mu\text{-Cl})Li(THF)_3$@SBA-1[f]	740	4.0	0.34	7.54	1.13	9.3	0.56	7.8
5g	$Fe^{III}[N(SiMe_3)_2]_2Cl(THF)$@SBA-1[f]	700	3.8	0.29	12.73	1.29	4.8	1.25	11.5

[a] Specific BET surface area. [b] Pore diameter calculated according to Ravikovich and Neimark;[93] all samples were pretreated at 250 °C (parent materials), 100 °C (silylated samples) and 25 °C (grafted samples) in vacuo until the pressure was $<10^{-3}$ Torr. [c] Pore volume determined at the relative pressure p/p_0 = 0.975. [d] Elemental analysis obtained after treatment at 100/25 °C (silylated/grafted samples) in vacuo ($<10^{-3}$ Torr). [e] Iron content from atom absorption spectroscopy (AAS) of HF treated samples. [f] Stirring time = 4 days.

known for alkyl ligands.[94] This behavior has been further examined by reacting $[Fe^{II}\{N(SiHMe_2)_2\}_2]_2$ (**9**) with a fully $SiHMe_2$-silylated MCM-41 sample (see Supporting Information). After 4 days at ambient temperature, decomposition had proceeded very slowly as revealed by iron analysis (0.49 wt %) of the recovered hybrid material. Also, the IR spectrum did not show any significant additional peaks, and the pore volume and BET surface changed only marginally.

Effect of the SBA-1 Pore Size. The implication of the window size of the SBA-1 system for the intrapore molecular diffusion and surface reaction was further studied by grafting ferrous precursor **9** onto a pore-enlarged SBA-1 material (**4**, D_{me} = 4.7 nm, a_s = 1260 m^2/g, V_p = 0.88 cm^3/g, 3.46 mmol SiOH/g Table 2, Figure 13).[77] As clearly revealed by DRIFT spectroscopy (Figure 12), after a reaction period of 18 h all silanol groups had been consumed in the resulting material $[Fe^{II}\{N(SiHMe_2)_2\}_2]_2$@SBA-1 (**4b**). Monopodally grafted iron centers are suggested as the predominant metal surface species (type **A** and **D**) by an N/Fe value of 1.05. Moreover, a higher iron content (6.1 wt %) and a C/N ratio of 6.8 indicate surface silylation involving species **K** to be less pronounced compared to the SBA-1 hybrid materials **3b**−**e**. This is also supported by the BET surface area, pore volume, and pore diameter of material **4b** which are considerably smaller than those found for $SiHMe_2$@SBA-1 (**4a**) (Table 2, Figure 13). However, diffusion of molecular complex **9** through pore-enlarged SBA-1 material (**4**) seems to be still restricted when comparing hybrid materials **4b** and **2b**, the latter involving a large channel-like pore system (Table 1). This distinct grafting behavior is further demonstrated for the surface reaction of bulky $Fe^{II}[N(SiPhMe_2)_2]_2$ (**7**) on SBA-1 **4**. Surface metalation is rather incomplete (iron content 2.6 wt %) and π-interactions of the phenyl rings with free silanol groups are pronounced (3624 cm^{-1}, Figure 12). Furthermore, the BET surface area,

dx.doi.org/10.1021/ic200788f |*Inorg. Chem.* 2011, 50, 7217–7228

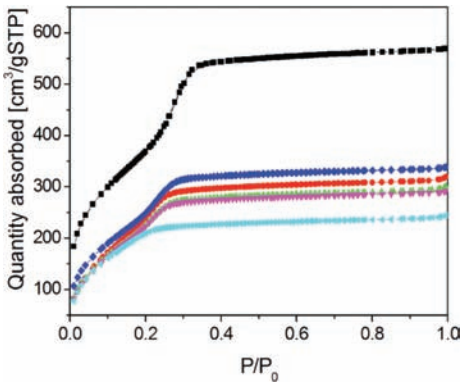

Figure 9. Nitrogen adsorption/desorption isotherms of SBA-1 (**3**, black solid squares), $SiHMe_2$@SBA-1 (**3a**, red solid circles), $[Fe^{II}\{N(SiHMe_2)_2\}_2]_2$@SBA-1 (**3b**, green solid triangles; solvent: hexane, 18 h reaction time), $[Fe^{II}\{N(SiHMe_2)_2\}_2]_2$@SBA-1 (**3c**, blue solid diamonds; solvent: thf, 18 h reaction time), $[Fe^{II}\{N(SiHMe_2)_2\}_2]_2$@SBA-1 (**3d**, magenta solid triangles; solvent: toluene, 18 h reaction time), and $[Fe^{II}\{N(SiHMe_2)_2\}_2]_2$@SBA-1 (**3e**, turquoise solid triangles; solvent: hexane, 4 d reaction time).

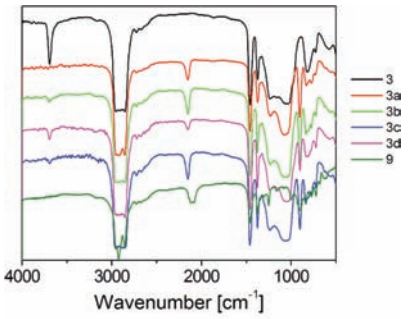

Figure 10. IR spectra (Nujol) of mesoporous silica SBA-1 (**3**), hybrid materials **3a**, **3b**, **3c**, **3d** as well as precursor $[Fe^{II}\{N(SiHMe_2)_2\}_2]_2$ (**9**).

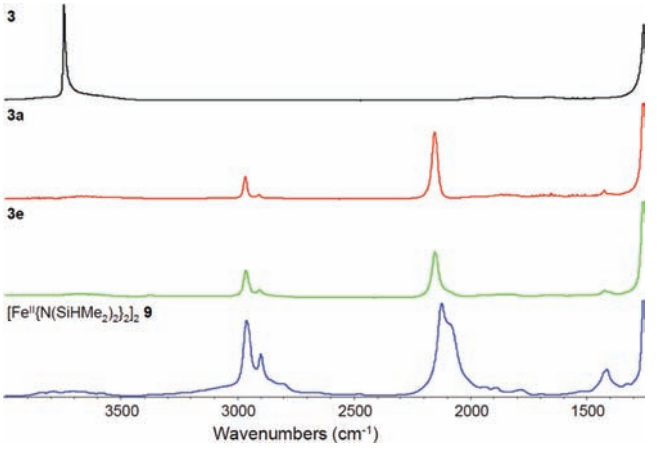

Figure 11. IR spectra (DRIFT) of mesoporous silica SBA-1 (**3**), hybrid materials **3a** and **3e** as well as precursor $[Fe^{II}\{N(SiHMe_2)_2\}_2]_2$ (**9**) in the range of 1300−4000 cm^{-1} (for the range of 400−4000 cm^{-1}, see Supporting Information).

(calculated) pore diameter, and pore volume are in the same range as of silylated material **4a**. This is in sharp contrast to hybrid material $Fe^{II}[N(SiPhMe_2)_2]_2$@MCM-41 (**2b**) which

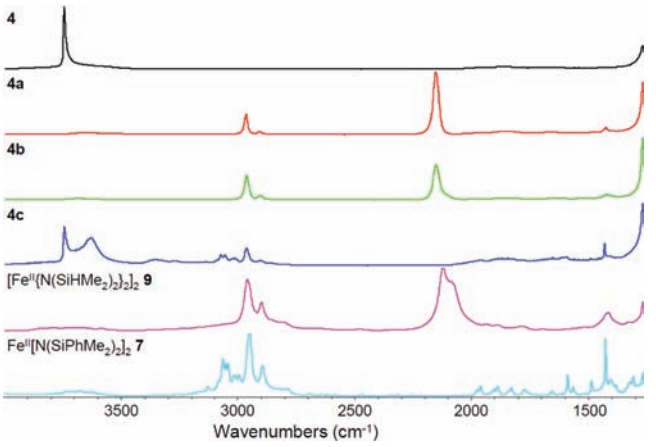

Figure 12. IR spectra (DRIFT) of mesoporous silica SBA-1 (**4**), hybrid materials **4a**, **4b**, and **4c** as well as precursors $[Fe^{II}\{N(SiHMe_2)_2\}_2]_2$ (**9**) and $Fe^{II}[N(SiPhMe_2)_2]_2$ (**7**) in the range of 1300−4000 cm^{-1} (for the range of 400−4000 cm^{-1}, see Supporting Information).

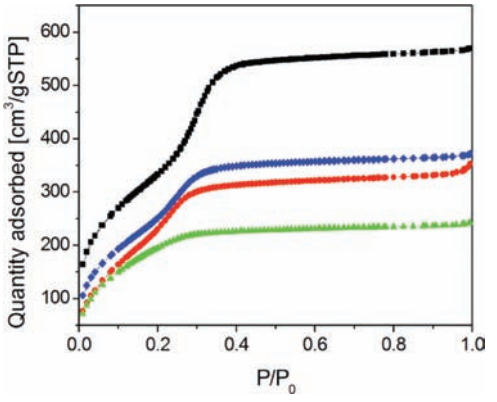

Figure 13. Nitrogen adsorption/desorption isotherms of SBA-1 (**4**, black solid squares), $SiHMe_2$@SBA-1 (**4a**, red solid circles), $[Fe^{II}\{N(SiHMe_2)_2\}_2]_2$@SBA-1 (**4b**, green solid triangles), and $Fe^{II}[N(SiPhMe_2)_2]_2$@SBA-1 (**4c**, blue solid diamonds).

shows a much higher surface coverage (iron content 9.7 wt %, Table 1).

Effect of the Molecular Iron Precursor. To demonstrate that the size-selective behavior of the SBA-1 support material is not $[Fe^{II}\{N(SiHMe_2)_2\}_2]_2$-sensitive, we further studied the surface grafting of another ferrous precursor, $Fe^{II}[N(SiMe_3)_2]_2(THF)$ (**6**)[70] and the two ferric complexes $Fe^{III}[N(SiMe_3)_2]_2Cl(THF)$ (**8**)[72] and $Fe^{III}[N(SiHMe_2)_2]_3(\mu\text{-}Cl)Li(THF)_3$ (**10**). As observed for hybrid materials $[Fe^{II}\{N(SiHMe_2)_2\}_2]_2$@SBA-1 (**3b**−**e**), complexes **6**, **8**, and **10** did not consume all silanol groups of a standard SBA-1 sample (**5**, D_{me} = 4.5 nm, a_s = 1320 m^2/g, V_p = 0.82 cm^3/g, 3.28 mmol SiOH/g Table 2, Figure 14) by conducting the reaction in hexane for 18 h.

The iron load (1.2 wt %) and the relatively high N/Fe ratio of 1.16 of ferrous material **5b** point to **F** (Figure 6) as the main surface species, while the ferric materials **5c** and **5d** feature iron contents (0.97 and 3.3 wt %) and ratios N/Fe <1, suggesting bipodally grafted iron centers of type **I**(THF) as major components. The high C/N ratios of up to 51 as well as the physisorption data (Figure 14) also reflect surface silylation (species **L**) and THF coordination to be prevalent. Interestingly, the iron content

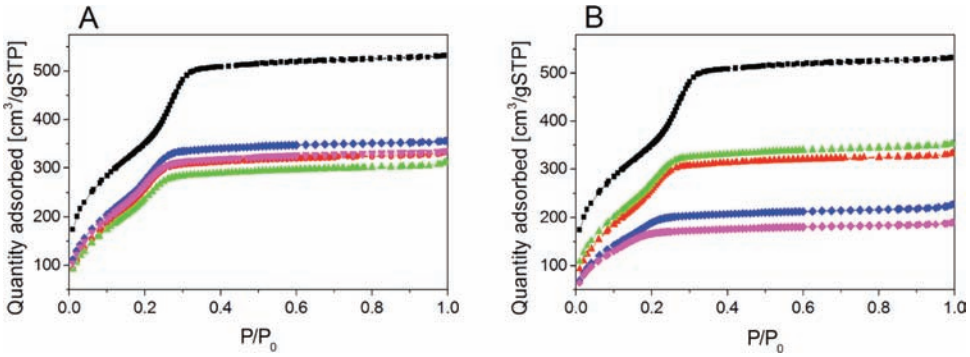

Figure 14. Nitrogen adsorption/desorption isotherms of SBA-1 (**5**, black solid squares), $SiHMe_2$@SBA-1 (**5a**, red solid circles), $Fe^{II}[N(SiMe_3)_2]_2$(THF)@SBA-1 (**5b**, green solid triangles), $Fe^{III}[N(SiHMe_2)_2]_3(\mu$-Cl)Li(THF)$_3$@SBA-1 (**5c**, blue solid diamonds), and $Fe^{III}[N(SiMe_3)_2]_2$Cl(THF)@SBA-1 (**5d**, magenta solid triangles) after 18 h (A left) and 4 d grafting time (B right).

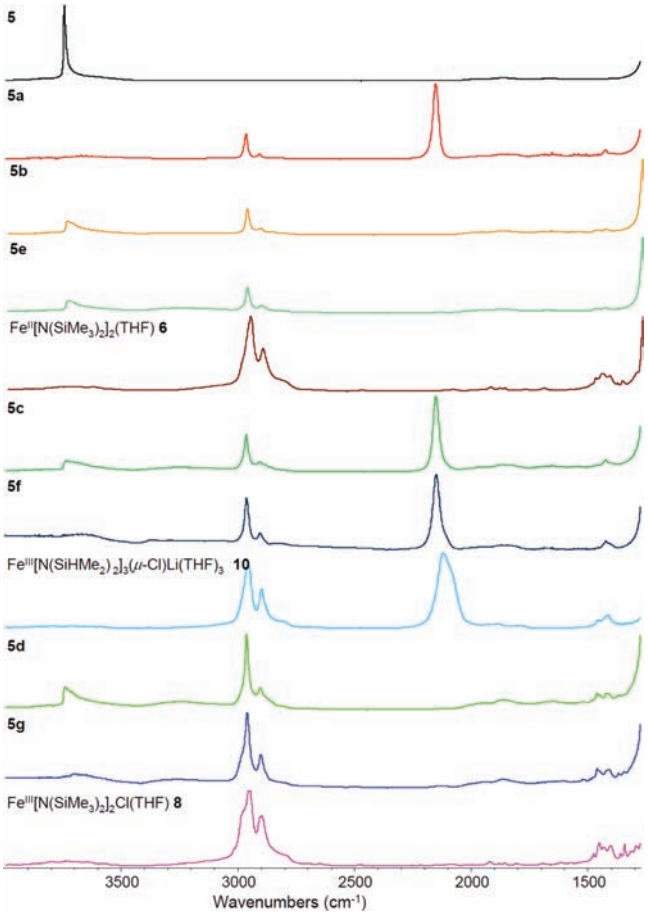

Figure 15. IR spectra (DRIFT) of mesoporous silica SBA-1 **5** and hybrid materials **5a**−**5f**, as well as precursors $Fe^{II}[N(SiMe_3)_2]_2$(THF) (**6**), $Fe^{III}[N(SiHMe_2)_2]_3(\mu$-Cl)Li(THF)$_3$ (**10**), and $Fe^{III}[N(SiMe_3)_2]_2$Cl(THF) (**8**) in the range of 1300−4000 cm^{-1} (for the range of 400−4000 cm^{-1}, see Supporting Information).

of the ferric hybrid materials $Fe^{III}[N(SiHMe_2)_2]_3(\mu$-Cl)Li(THF)$_3$@SBA-1 (**5f**) and $Fe^{III}[N(SiMe_3)_2]_2$Cl(THF)@SBA-1 (**5g**) increased dramatically to 9.3 and 4.8 wt % after a reaction time of 4 d. Higher surface metalation and less surface silylation is also indicated by relatively small C/N ratios of 7.8 (**5f**) and 11.5 (**5g**) and considerably decreased BET surface areas, (calculated) pore diameters, and pore volumes compared to materials **5c** and **5d** (both obtained after 18 h reaction time). The DRIFT spectra of **5f** and **5g** revealed >95% consumption of the silanol groups (Figure 15).

It is noteworthy that the N/Fe ratio of the ferric materials $Fe^{III}[N(SiMe_3)_2]_2$Cl(THF)@SBA-1 seem to have considerably increased after the prolonged reaction time (**5d**: 0.40 versus **5g**: 1.25) while those for $Fe^{III}[N(SiHMe_2)_2]_3(\mu$-Cl)Li(THF)$_3$@SBA-1 changed only marginally (**5c**: 0.66 versus **5f**: 0.56). Hence, material $Fe^{III}[N(SiMe_3)_2]_2$Cl(THF)@SBA-1 (**5g**) might be mainly represented by species **J** (Figure 6). Except for **5e**, a longer reaction time leads to a lower silylation degree (Table 2).

Finally, the local environment of iron(III) centers incorporated into siliceous materials has been extensively studied by means of electron paramagnetic resonance (EPR) spectroscopy.[29,30,40,95−101] We have recorded the X-band EPR spectra of two representative materials including their ferrous and ferric silylamide precursors (Figure 16). The EPR spectrum of complex $Fe^{III}[N(SiMe_3)_2]_2$Cl(THF) (**8**, A) displays three signals with g values of 9.1, 4.3, and 2.0. For comparison, siloxide complex $Fe^{III}[OSi(OtBu)_3]_3$(THF) showed signals at g = 5.5 and 2.0,[28] indicative of a 4-coordinate, high-spin Fe^{3+} in a C_{3v} environment ($g_\perp \approx 6$ and $g_\parallel \approx 2$).[99,101] The EPR spectrum of grafted ferric material $Fe^{III}[N(SiMe_3)_2]_2$Cl(THF)@SBA-1 (**5g**) is similar to that of the precursor revealing two major components at g = 9.1 and 4.3, which can be attributed to Fe^{3+} species in a highly distorted tetrahedral environment.[40,99,100] Particularly, the ferric centers of bipodally grafted species **I**(THF) are anticipated to exhibit a considerably distorted coordination geometry. Interestingly, for material **5g**, the peak at g = 2.0, which has been previously assigned to undistorted tetrahedral Fe^{3+} sites,[95] disappeared completely. Fe(II) species were reported to display no significant resonance at ambient temperature. We found that ferrous dinuclear precursor $[Fe^{II}\{N(SiHMe_2)_2\}_2]_2$ (**9**) shows a very broad signal (Figure 16, B), which is shifted to higher g values for the grafted material $[Fe^{II}\{N(SiHMe_2)_2\}_2]_2$@MCM-41 (**1b**). It is noteworthy that g values of 2.2−2.5 have been associated with small iron oxide domains.[95−97]

■ CONCLUSIONS

The immobilization of ferrous and ferric silylamide complexes on periodic mesoporous silica (PMS) materials is a feasible route to generate surface-bonded iron species in a hydrophobic

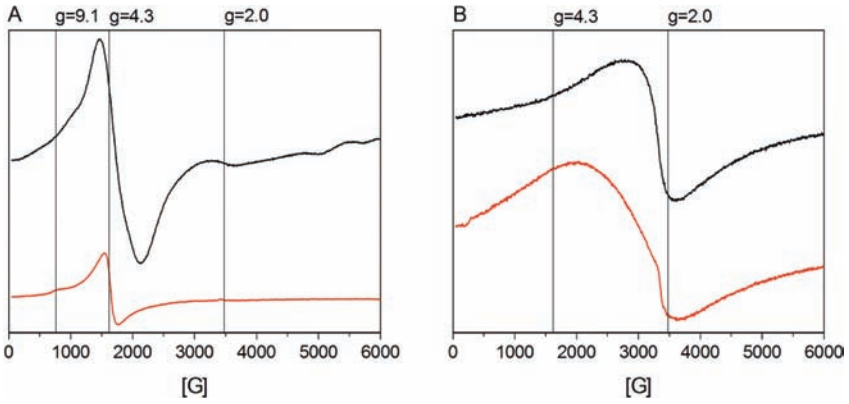

Figure 16. X-Band EPR spectra at ambient temperature of (A) precursor $Fe^{III}[N(SiMe_3)_2]_2Cl(THF)$ (**8**, black solid lines) and material $Fe^{III}[N(SiMe_3)_2]_2Cl(THF)$@SBA-1 (**5g**, red solid lines) and (B) precursor $[Fe^{II}\{N(SiHMe_2)_2\}_2]_2$ (**9**, black solid lines) and material $[Fe^{II}\{N(SiHMe_2)_2\}_2]_2$@MCM-41 (**1b**, red solid lines).

microenvironment (via competitive surface silylation). Tailor-made complexes $[Fe^{II}\{N(SiHMe_2)_2\}_2]_2$ and $Fe^{III}[N(SiHMe_2)_2]_3$-(μ-Cl)Li(THF)$_3$ facilitate the elucidation of coexistent surface species such as O−Fe−N(SiHMe$_2$)$_2$ and O−SiHMe$_2$ because of the SiH moiety which acts as a significant IR-spectroscopic probe. Iron silylamide grafting onto the surface of MCM-41 featuring relatively large channel-like pores depends mainly on the type of iron precursor, that is, the iron loading and surface connectivity (mono- or bipodally grafted species) are controlled by the size of the silylamido ligand and the nuclearity of the iron complex (monoiron versus diiron). In contrast, pore blockage effects via predominant functionalization of the pore openings are observed in case of the cubic cage-like PMS material SBA-1. Since the pore-openings (cage windows) of a standard SBA-1 material are only slightly larger than the dimensions of the molecular iron precursors, the grafting reactions become diffusion-limited and hence, governed not only by the size of the iron precursor and proligand but also by the pore size, reaction time, and solvent. As a consequence lower metal loadings and a more pronounced surface silylation were found to be prominent for cage-like SBA-1. Such size-selective functionalization of PMS materials might be exploited for the design of bioinspired nanostructured catalysts featuring biologically relevant metal centers, so-called mesozymes.[52]

EXPERIMENTAL SECTION

General Materials. The syntheses of the metalorganic iron complexes and the grafting experiments were performed with rigorous exclusion of air and water, using high-vacuum (Schlenk) and glovebox techniques (MBraun MB150B-G; <1 ppm O_2, <1 ppm H_2O). Hexane, toluene, and THF were purified by using Grubbs columns (MBraun SPS, solvent purification system) and stored in a glovebox. Tetramethyldisilazane and 1,3-diphenyl-1,1,3,3-tetramethylsilazane were obtained from ABCR. Iron(II)- and iron(III) chloride (each ≥99.99%) were purchased from Sigma-Aldrich. Potassium bis(trimethylsilyl)amide was obtained from Aldrich and sublimed prior to use. Li[N(SiHMe$_2$)$_2$] and Li[N(SiPhMe$_2$)$_2$] were synthesized according to previously described protocols by reacting *n*-BuLi with 1,1,3,3-tetramethyldisilazane and 1,3-diphenyl-1,1,3,3-tetramethylsilazane, respectively.[102] Previously reported complexes $Fe^{II}[N(SiMe_3)_2]_2(THF)$ (**6**),[70] $Fe^{II}[N(SiPh_2Me_2)_2]_2$ (**7**),[71] and $Fe^{III}[N(SiMe_3)_2]_2Cl(THF)$ (**8**)[72] were synthesized according to salt metathesis protocols using modified literature procedures (details are available in the Supporting Information).

Iron Precursors. *$[Fe^{II}\{N(SiHMe_2)_2\}_2]_2$ (**9**).* A solution of LiN(SiHMe$_2$)$_2$ (4.40 g, 31.56 mmol) in 5 mL of THF was slowly added to a milky white solution of $FeCl_2$ (2.04 g, 15.78 mmol) in 5 mL of THF. Immediately, the mixture turned into a dark brown solution, and was evaporated to dryness after having been stirred for 1 h at ambient temperature. The residue was washed and centrifuged with *n*-hexane (3×), the dark green (almost black) *n*-hexane fractions collected, and the solvent removed. Subsequent crystallization from *n*-hexane at −35 °C yielded green single crystals of pure compound **9** (3.06 g, 9.56 mmol, 61%). Analysis calculated for $C_8H_{28}N_2Si_4Fe$: C 29.98, H 8.81, N 8.74. Found: C 29.49, H 9.01, N 8.46. ^{1}H NMR (500.13 MHz, d_8-toluene, 293 K): δ = −6.85 (s, 24H, $SiCH_3$), 6.97 (s, 24H, $SiCH_3$), 75.66 (s, 4H, SiH), 85.05 (s, 4H, SiH) ppm. DRIFT (KBr, KBr, cm^{-1}): 2949s, 2899 m, 2116s, 2083s, 1418w, 1250s, 1001 m, 889s, 839s, 804 m, 788 m, 773 m, 727w, 628w, 604w 472w.

*$Fe^{III}[N(SiHMe_2)_2]_3(\mu$-Cl)Li(THF)$_3$ (**10**).* A solution of LiN(SiHMe$_2$)$_2$ (1.20 g, 8.63 mmol) in 5 mL of THF was cooled to −35 °C and added slowly (***Caution!*** *highly exothermic reaction*) to a green solution of $FeCl_3$ (483 mg, 2.98 mmol) in 5 mL of THF (precooled to −35 °C). Already the first few drops caused a red color. After having been stirred for 2 h at ambient temperature, the solvent of the dark red solution was removed under reduced pressure. Combined *n*-hexane washings−centrifugations (3×) of the remaining solid and two recrystallizations from *n*-hexane at −35 °C yielded red orange crystals of **10** (1.09 g, 1.53 mmol, 53%). Analysis calculated for $C_{24}H_{66}N_3O_3Si_4ClFeLi$: C 40.51, H 9.35, N 5.91. Found: C 38.78, H 8.51, N 5.96. DRIFT (KBr, KBr, cm^{-1}): 2954s, 2899 m, 2120s, 1459vw, 1448vw, 1413w, 1248s, 1176vw, 1041w, 969 m, 894vs, 886vs, 843s, 836s, 804 m, 763 m, 696 m, 681 m, 643w, 426vw, 407vw.

Parent PMS Materials. Samples of periodic mesoporous silica SBA-1 and MCM-41 were synthesized according to recently published procedures.[63,103] Details of the syntheses and characterization data are given in the Supporting Information and Tables 1 and 2.

Hybrid Materials. *Surface Silylation of PMS Materials.* Dehydrated PMS (100 mg) was suspended in 5 mL of *n*-hexane and, under stirring, excess of 1,1,3,3-tetramethyldisilazane (200 mg, 1.50 mmol) was added. The mixture was stirred for 18 h at ambient temperature, and nonreacted silazane separated via combined *n*-hexane washings−centrifugations (3×). Subsequent removal of the solvent under vacuum yielded the hybrid materials SiHMe$_2$@MCM-41 (**1a**; isolated: 91 mg; analysis found: C 7.08, H 1.86, N 0.15), SiHMe$_2$@MCM-41 (**2a**; 86 mg; C 6.94, H 1.59, N 0.05), SiHMe$_2$@SBA-1 (**3a**; 81 mg; C 7.36, H 1.90, N 0.02), SiHMe$_2$@SBA-1 (**4a**; 102 mg; C 6.92, H 2.39, N 0.00), and SiHMe$_2$@SBA-1 (**5a**; 100 mg; C 6.61, H 1.45, N, 0.11). Further characterization data are given in Tables 1 and 2 and Figures 4, 5 and 7−15.

dx.doi.org/10.1021/ic200788f |*Inorg. Chem.* 2011, 50, 7217–7228

Grafting of Iron Silylamide Complexes onto PMS Materials. Dehydrated PMS (**1**−**5**) was suspended in 5 mL of *n*-hexane (if not otherwise noted), and a solution of iron silylamide in *n*-hexane added. The mixture was stirred for 18 h (if not otherwise noted) at ambient temperature, and the hybrid material separated from any solubles (released silylamine, nonreacted iron precursor) via combined *n*-hexane washings−centrifugations (3×). Finally, the solvent was removed in vacuo.

Fe^{II}[N(SiHMe$_2$)$_2$]$_2$@MCM-41 (***1b***). MCM-41 (**1**, 113 mg) and **9** (147 mg, 0.459 mmol) gave a yellowish/brownish mixture which turned black. Brown hybrid material (**1b**; 193 mg; C 10.54, H 2.28, N 3.22, Fe 12.8) and a black oil (20 mg, nonreacted precursor **9**).

Fe^{III}[N(SiHMe$_2$)$_2$]$_3$(μ-Cl)Li(THF)$_3$@MCM-41 (***1c***). MCM-41 (**1**, 99 mg) and **10** (275 mg, 0.386 mmol) gave a dark orange mixture which turned slightly brown. Orange brownish hybrid material (**1c**; 129 mg; C 11.50, H 2.59, N 1.66, Fe 6.2) and dark brown oil (92 mg, nonreacted precursor **10**).

Fe^{II}[N(SiPhMe$_2$)$_2$]$_2$@MCM-41 (***2b***). MCM-41 (**2**, 160 mg) and **7** (375 mg, 0.61 mmol) gave a yellowish mixture which turned slightly brownish. Yellow hybrid material (**2b**; 187 mg; C 21.89, H 2.83, N 0.67, Fe 9.7). Excess of the nonreacted iron precursor **7** was recovered as azure crystals upon crystallization from *n*-hexane.

Fe^{II}{N(SiHMe$_2$)$_2$}$_2$]$_2$@SBA-1 (***3b***). SBA-1 (**3**, 108 mg) and **9** (158 mg, 0.49 mmol) gave a yellow-brownish mixture which turned black. Beige hybrid material (**3b**; 134 mg; C 6.62, H 1.65, N 0.57, Fe, 2.3) and a black oil.

Fe^{II}{N(SiHMe$_2$)$_2$}$_2$]$_2$@SBA-1 (***3c***). SBA-1 (**3**, 159 mg) and **9** (210 mg, 0.66 mmol) in THF gave a brownish mixture which turned black. Beige hybrid material (**3c**; 196 mg; C 12.08, H 1.53, N 0.39; Fe 3.3) and a black oil.

Fe^{II}{N(SiHMe$_2$)$_2$}$_2$]$_2$@SBA-1 (***3d***). SBA-1 (**3**, 115 mg) and **9** (162 mg (0.51 mmol) in toluene gave a yellowish mixture which turned black. Beige hybrid material (**3d**; 103 mg; C 7.14, H 3.44, N 0.00, Fe 2.4) and a black oil.

Fe^{II}{N(SiHMe$_2$)$_2$}$_2$]$_2$@SBA-1 (***3e***). SBA-1 (**3**, 191 mg) and **9** (257 mg, 0.80 mmol) in *n*-hexane gave a yellow-brownish mixture which turned black (4 d). Brown hybrid material (**3e**; 221 mg; C 9.67, H 2.71, N 1.45, Fe 4.7) and a black oil.

Fe^{II}{N(SiHMe$_2$)$_2$}$_2$]$_2$@SBA-1 (***4b***). SBA-1 (**4**, 191 mg) and **9** (257 mg, 0.80 mmol) in *n*-hexane gave a yellow-brownish mixture which turned black (4 d). Brown hybrid material (**4b**; 221 mg; C 9.44, H 3.57, N 1.61, Fe 6.1) and a black oil.

Fe^{II}[N(SiPhMe$_2$)$_2$]$_2$@SBA-1 (***4c***). SBA-1 (**4**, 210 mg) and **7** (644 mg, 1.05 mmol) in *n*-hexane gave a light yellow mixture which turned slightly brownish. Yellow hybrid material (**4c**; 187 mg; C 10.48, H 3.78, N 0.34, Fe 2.6). Excess of the nonreacted iron precursor **6** was recovered as azure crystals (450 mg, 0.74 mmol, 70%) upon crystallization from *n*-hexane.

Fe^{II}[N(SiMe$_3$)$_2$]$_2$(THF)@SBA-1 (***5b***). SBA-1 (**5**, 151 mg) and **6** (207 mg, 0.53 mmol) in *n*-hexane gave a dark green mixture. Gray hybrid material (**5b**; 135 mg; C 6.66, H 2.99, N 0.05, Fe 1.2.) and dark green oil (146 mg, 0.37 mmol, 71% of the nonreacted precursor).

Fe^{III}[N(SiHMe$_2$)$_2$]$_3$(μ-Cl)Li(THF)$_3$@SBA-1 (***5c***). SBA-1 (**5**, 61 mg) and **10** (155 mg, 0.22 mmol) in *n*-hexane gave an orange mixture which turned brown. Beige-brownish hybrid material (**5c**; 73 mg; C 6.47, H 2.73, N 0.22, Fe 0.97) and black oil (65 mg).

Fe^{III}[N(SiMe$_3$)$_2$]$_2$Cl(THF)@SBA-1 (***5d***). SBA-1 (**5**, 153 mg) and **8** (278 mg, 0.57 mmol) in *n*-hexane gave a dark purple mixture which turned slightly black. Orange-brownish hybrid material (**5d**; 186 mg; C 9.43, H 3.20, N 0.18, Fe 3.3) and purple crystals of **8** (168 mg, 0.34 mmol).

Fe^{II}[N(SiMe$_3$)$_2$]$_2$(THF)@SBA-1 (***5e***). SBA-1 (**5**, 150 mg) and **6** (278 mg, 0.62 mmol) in *n*-hexane gave a dark green mixture (4 d). Gray hybrid material (**5e**; 135 mg; C, 7.65; H, 1.97; N, 0.25; Fe, 1.9) and a dark green oil (86 mg, 0.19 mmol of nonreacted precursor **6**).

Fe^{III}[N(SiHMe$_2$)$_2$]$_3$(μ-Cl)Li(THF)$_3$@SBA-1 (***5f***). SBA-1 (**5**, 130 mg) and **10** (456 mg, 0.64 mmol) in *n*-hexane gave a orange mixture which turned brown (4 d). Dark brown hybrid material (**5f**; 196 mg; C 7.54, H 2.17, N 1.13, Fe 9.3) and a black oil (145 mg).

Fe^{III}[N(SiMe$_3$)$_2$]$_2$Cl(THF)@SBA-1 (***5g***). SBA-1 (**5**, 165 mg) and **8** (393 mg, 0.81 mmol) in *n*-hexane gave a dark purple solution which turned slightly black (4 d). Orange-brown hybrid material (**5g**; 199 mg; C 9.89, H 2.96, N 1.29, Fe 4.8) and purple crystals (183 mg, 0.43 mmol, 47% of nonreacted precursor **8**).

Table 3. Crystal Data and Data Collection Parameters of Complexes 9 and 10

	9	**10**
chemical formula	$C_{16}H_{56}N_4Si_8Fe_2$	$C_{24}H_{66}N_3O_3Si_6ClFeLi$
M_r	641.07	711.58
crystal system	triclinic	monoclinic
space group	$P\bar{1}$	$P2_1/c$
a/Å	8.7407(10)	16.977(2)
b/Å	9.6694(11)	11.7625(17)
c/Å	11.8888(14)	20.708(3)
α/deg	92.662(2)	90
β/deg	104.056(2)	92.868(3)
γ/deg	110.779(2)	90
V/Å^3	901.53(18)	4130.1(10)
Z	1	4
F(000)	344	1540
T/K	123(2)	123(2)
ρ_{calcd}/g cm^{-3}	1.181	1.144
μ/mm^{-1}	1.082	0.630
R_1 (obsd)[a]	0.0489 (4042)	0.0759 (10958)
wR_2 (all)[a]	0.1415	0.2175
GOF(obsd)	1.069	1.093

[a] $R_1 = \Sigma||F_o| - |F_c||/\Sigma|F_o|$; $wR_2 = \{\Sigma w(F_o^2 - F_c^2)^2/\Sigma w(F_o^2)^2]\}^{1/2}$; GOF = $\{\Sigma[w(F_o^2 - F_c^2)^2]/(n-p)\}^{1/2}$.

Characterization. ^{1}H NMR spectra of the iron silylamide complexes were recorded at 25 °C in d_8-toluene (if not otherwise noted) on a Bruker AV II+ 500 (^{1}H: 500.13 MHz). Shifts are reported in parts per million relative to TMS. Powder X-ray diffraction (PXRD) patterns were recorded on a Bruker D8 ADVANCE instrument in the step/scan mode (step width = 0.00825; accumulation time = 2 s/step; range (2θ) = 0.50−10.00°) using monochromatic CuK$_{\alpha 1}$ radiation (λ = 1.540562 Å. IR spectra were recorded on a Nicolet Impact 410 FT-IR spectrometer using Nujol mulls sandwiched between CsI plates. DRIFT spectra were obtained on a Nicolet 6700 FT-IR spectrometer using dried KBr powder and KBr windows. EPR measurements were performed on a Bruker ESR 300E spectrometer with 100 kHz field modulation at ambient temperature. Nitrogen adsorption/desorption isotherms were measured with an ASAP 2020 volumetric adsorption apparatus (Micromeritics) at 77.4 K for relative pressures from 1×10^{-2} to 0.99 (a_m(N$_2$, 77 K) 0.162 nm^2). The BET specific surface area was obtained from the nitrogen adsorption data in the relative pressure range from 0.1 to 0.15 for SBA-1 materials and from 0.1 to 0.2 for MCM-41 materials.[104,105] The pore size distributions were calculated using the Barrett−Joyner−Halenda (BJH) method.[106] Although the BJH method systematically underestimates the effective pore diameter of cage-like materials, it gives a good measure of relative changes of the pore size.[78] In addition, the cage diameters of the parent and hybrid SBA-1 materials were calculated according to the "model of spherical cavities" using equation $D_{me} = a(6\varepsilon_{me}/\pi\upsilon)^{1/3}$, which has been proposed by Ravikovitch and Neimark.[93] D_{me} is the diameter of the cavities within the unit cell of length a, ε_{me} is the volume fraction of a regular cavity, $\varepsilon_{me} = \rho_v V_{me}/(1 + \rho_v V_{me})$, where ρ_v = 2.2 g cm^{-3} is the estimated silica wall density and υ is the number of

dx.doi.org/10.1021/ic200788f |*Inorg. Chem.* 2011, 50, 7217–7228

cavities per unit cell (for the space group *Pm3n*, $v = 8$). Elemental analyses were performed on an Elementar VarioEL III instrument. Metal contents were measured via matrix-calibrated ICP-OES by Wessling Laboratories GmbH, Münster, Germany. The surface silanol population was obtained from the surface coverage (SiR_3) of activated (250 °C, 3 h, 1×10^{-2} Torr) silylated samples as described previously.[91]

X-ray Crystallography and Crystal Structure Determination of Complexes 9 and 10. Crystals were grown by standard techniques from saturated solutions using hexane at −35 °C. Suitable crystals for diffraction experiments were selected in a glovebox and mounted in Paratone-N (Hampton Research) inside a nylon loop. Data collection was done on a Bruker AXS SMART 2K CCD diffractometer, using graphite monochromated MoK_α radiation (λ = 0.71073 Å) performing 182° ω scans in four orthogonal φ positions. Structure solution and final model refinement was done using SHELXS97 and SHELXL-97.[107] All plots were generated using the program ORTEP-3.[108] Further details of the refinement and crystallographic data are listed in Table 3, and in CIF files; CCDC reference numbers 819456 and 819457.

■ ASSOCIATED CONTENT

Supporting Information. Detailed synthesis procedures, PXRD patterns, nitrogen physisorption isotherms, IR spectra, and crystallographic information files (CIF). This material is available free of charge via the Internet at http://pubs.acs.org.

■ AUTHOR INFORMATION

Corresponding Author

*E-mail: reiner.anwander@uni-tuebingen.de. Fax: +497071292436.

■ ACKNOWLEDGMENT

This research was supported by the NANOSCIENCE program of the University of Bergen. Special thanks go to Dorothea Schädle for conducting the VT NMR experiment and to Paul Schuler for recording the EPR spectra.

■ REFERENCES

(1) Bolm, C.; Legros, J.; Le Paih, J.; Zani, L. *Chem. Rev.* **2004**, *104*, 6217–6254.
(2) Enthaler, S.; Junge, K.; Beller, M. *Angew. Chem., Int. Ed.* **2008**, *47*, 3317–3321.
(3) Bolm, C. *Nat. Chem.* **2009**, *1*, 420.
(4) Garcia Mancheno, O. *Angew. Chem., Int. Ed.* **2011**, *50*, 2216–2218.
(5) Britovsek, G. J. P.; Gibson, V. C.; Kimberley, B. S.; Maddox, P. J.; McTavish, S. J.; Solan, G. A.; White, A. J. P.; Williams, D. J. *Chem. Commun.* **1998**, 849–850.
(6) Small, B. L.; Brookhart, M. *J. Am. Chem. Soc.* **1998**, *120*, 7143–7144.
(7) Plietker, B., Ed.; *Iron Catalysis in Organic Chemistry Reactions and Applications*; Wiley-VCH: Weinheim, Germany, 2008.
(8) Sherry, B. D.; Fürstner, A. *Acc. Chem. Res.* **2008**, *41*, 1500–1511.
(9) Sun, C.-L.; Li, B.-J.; Shi, Z.-J. *Chem. Rev.* **2011**, *111*, 1293–1314.
(10) Zhu, S.-F.; Cai, Y.; Mao, H.-X.; Xie, J.-H.; Zhou, Q.-L. *Nat. Chem.* **2010**, *2*, 546–551.
(11) Chen, M. S.; White, M. C. *Science* **2010**, *327*, 566–571.
(12) Federsel, C.; Boddien, A.; Jackstell, R.; Jennerjahn, R.; Dyson, P. J.; Scopelliti, R.; Laurenczy, G.; Beller, M. *Angew. Chem., Int. Ed.* **2010**, *49*, 9777–9780.
(13) Yang, J.; Tilley, T. D. *Angew. Chem., Int. Ed.* **2010**, *49*, 10186–10188.
(14) Zecchina, A.; Groppo, E.; Bordiga, S. *Chem.—Eur. J.* **2007**, *13*, 2440–2460.
(15) Jennings, J. R., Ed.; *Catalytic Ammonia Synthesis. Fundamentals and Practice*; Plenum Press: New York, 1991.
(16) Costas, M.; Mehn, M. P.; Jensen, M. P.; Que, L., Jr. *Chem. Rev.* **2004**, *104*, 939–986.
(17) Collman, J. P.; Boulatov, R.; Sunderland, C. J.; Fu, L. *Chem. Rev.* **2004**, *104*, 561–588.
(18) Tame, J. *Chem. Rev.* **1992**, *2*, 26–31.
(19) Lipscomb, J. D.; Que, L., Jr. *J. Biol. Inorg. Chem.* **1998**, *3*, 331–336.
(20) Fox, B. G.; Lyle, K. S.; Rogge, C. E. *Acc. Chem. Res.* **2004**, *37*, 421–429.
(21) Merkx, M.; Kopp, D. A.; Sazinsky, M. H.; Blazyk, J. L.; Muller, J.; Lippard, S. J. *Angew. Chem., Int. Ed.* **2001**, *40*, 2782–2807.
(22) Lukin, J. A.; Ho, C. *Chem. Rev.* **2004**, *104*, 1219–1230.
(23) Baik, M.-H.; Newcomb, M.; Friesner, R. A.; Lippard, S. J. *Chem. Rev.* **2003**, *103*, 2385–2419.
(24) Dance, I. *Dalton Trans.* **2010**, *39*, 2972–2983.
(25) Liu, P.; Zhou, C.-Y.; Xiang, S.; Che, C.-M. *Chem. Commun.* **2010**, *46*, 2739–2741.
(26) Kaul, F. A. R.; Puchta, G. T.; Schneider, H.; Bielert, F.; Mihalios, D.; Herrmann, W. A. *Organometallics* **2002**, *21*, 74–82.
(27) Piovezan, C.; Jovito, R.; Bortoluzzi, A. J.; Terenzi, H.; Fischer, F. L.; Severino, P. C.; Pich, C. T.; Azzolini, G. G.; Peralta, R. A.; Rossi, L. M.; Neves, A. *Inorg. Chem.* **2010**, *49*, 2580–2582.
(28) Nozaki, C.; Lugmair, C. G.; Bell, A. T.; Tilley, T. D. *J. Am. Chem. Soc.* **2002**, *124*, 13194–13203.
(29) Holland, A. W.; Li, G.; Shahin, A. M.; Long, G. J.; Bell, A. T.; Tilley, T. D. *J. Catal.* **2005**, *235*, 150–163.
(30) Roukoss, C.; Fiddy, S.; de Mallmann, A.; Rendon, N.; Basset, J.-M.; Kuntz, E.; Coperet, C. *Dalton Trans.* **2007**, 5546–5548.
(31) Roukoss, C.; Basset, J.-M.; Coperet, C.; Lucas, C.; Kuntz, E. *C. R. Chim.* **2008**, *11*, 620–627.
(32) Costa, A. A.; Ghesti, G. F.; de Macedo, J. L.; Braga, V. S.; Santos, M. M.; Dias, J. A.; Dias, S. C. L. *J. Mol. Catal., A: Chem.* **2008**, *282*, 149–157.
(33) Figueiredo, H.; Silva, B.; Raposo, M. M. M.; Fonseca, A. M.; Neves, I. C.; Quintelas, C.; Tavares, T. *Microporous Mesoporous Mater.* **2008**, *109*, 163–171.
(34) Liu, F.; John, K. D.; Scott, B. L.; Baker, R. T.; Ott, K. C.; Tumas, W. *Angew. Chem., Int. Ed.* **2000**, *39*, 3127–3130.
(35) Long, J.; Zhang, Z.; Ding, Z.; Ruan, R.; Li, Z.; Wang, X. *J. Phys. Chem. C* **2010**, *114*, 15713–15727.
(36) Wang, X.; Long, J.; Yan, G.; Zhang, G.; Fu, X.; Basset, J.-M.; Lefebvre, F. *Microporous Mesoporous Mater.* **2008**, *108*, 258–265.
(37) Long, J.; Wang, X.; Zhang, G.; Dong, J.; Yan, T.; Li, Z.; Fu, X. *Chem.—Eur. J.* **2007**, *13*, 7890–7899.
(38) Long, J.; Wang, X.; Ding, Z.; Zhang, Z.; Lin, H.; Dai, W.; Fu, X. *J. Catal.* **2009**, *264*, 163–174.
(39) Vinu, A.; Krithiga, T.; Murugesan, V.; Hartmann, M. *Adv. Mater.* **2004**, *16*, 1817–1821.
(40) Vinu, A.; Nandhini, K. U.; Murugesan, V.; Böhlmann, W.; Umamaheswari, V.; Pöppl, A.; Hartmann, M. *Appl. Catal., A* **2004**, *265*, 1–10.
(41) Vinu, A.; Krithiga, T.; Balasubramanian, V. V.; Asthana, A.; Srinivasu, P.; Mori, T.; Ariga, K.; Ramanath, G.; Ganesan, P. G. *J. Phys. Chem. B* **2006**, *110*, 11924–11931.
(42) Li, Y.; Xia, H.; Fan, F.; Feng, Z.; van Santen, R. A.; Hensen, E. J. M.; Li, C. *Chem. Commun.* **2008**, 774–776.
(43) Liu, Y.-M.; Xu, J.; He, L.; Cao, Y.; He, H.-Y.; Zhao, D.-Y.; Zhuang, J.-H.; Fan, K.-N. *J. Phys. Chem. C* **2008**, *112*, 16575–16583.
(44) Brzozowski, R.; Vinu, A.; Gil, B. *Appl. Catal., A* **2010**, *377*, 76–82.
(45) Hugues, F.; Bassett, J. M.; Taarit, Y. B.; Choplin, A.; Primet, M.; Rojas, D.; Smith, A. K. *J. Am. Chem. Soc.* **1982**, *104*, 7020–7024.
(46) Schuenemann, V.; Trautwein, A. X.; Rietjens, I. M. C. M.; Boersma, M. G.; Veeger, C.; Mandon, D.; Weiss, R.; Bahl, K.; Colapietro, C.; Piech, M.; Austin, R. N. *Inorg. Chem.* **1999**, *38*, 4901–4905.
(47) De Stefanis, A.; Kaciulis, S.; Pandolfi, L. *Microporous Mesoporous Mater.* **2007**, *99*, 140–148.

(48) Haldar, S.; Koner, S. *J. Org. Chem.* **2010**, *75*, 6005–6008.
(49) Chen, H.-Y.; Sachtler, W. M. H. *Catal. Today* **1998**, *42*, 73–83.
(50) Panov, G. I.; Uriarte, A. K.; Rodkin, M. A.; Sobolev, V. I. *Catal. Today* **1998**, *41*, 365–385.
(51) Sobolev, V. I.; Dubkov, K. A.; Panna, O. V.; Panov, G. I. *Catal. Today* **1995**, *24*, 251–252.
(52) Anwander, R. *Chem. Mater.* **2001**, *13*, 4419–4438.
(53) Basset, J. M.; Choplin, A. *J. Mol. Catal.* **1983**, *21*, 95–108.
(54) Scott, S. L.; Basset, J. M.; Niccolai, G. P.; Santini, C. C.; Candy, J. P.; Lecuyer, C.; Quignard, F.; Choplin, A. *New J. Chem.* **1994**, *18*, 115–122.
(55) Iwasawa, Y. *Adv. Catal.* **1987**, *35*, 187–264.
(56) Anwander, R. *Top. Curr. Chem.* **1996**, *179*, 33–112.
(57) Anwander, R. Immobilization of Molecular Catalysts. In *Handbook of Heterogeneous Catalysis*, 2nd ed.; VCH Verlagsgesellschaft mbG: Weinheim, Germany, 2008; pp 583−614.
(58) Harris, D. H.; Lappert, M. F. *J. Organomet. Chem. Libr.* **1976**, *2*, 13–102.
(59) Bradley, D. C.; Chisholm, M. H. *Acc. Chem. Res.* **1976**, *9*, 273–280.
(60) Lappert, M. F.; Sanger, A. R.; Srivastava, R. C.; Power, P. P. *Metal and Metalloid Amides: Synthesis, Structure, and Physical and Chemical Properties*; Horwood−Wiley: Chichester, U.K., 1980; pp 1−848.
(61) Lappert, M. F.; Protchenko, A. V.; Power, P. P.; Seeber, A. L. *Metal Amide Chemistry*; John Wiley & Sons, Ltd: Chichester, U.K., 2008; pp 1−370.
(62) Anwander, R. *Top. Organomet. Chem.* **1999**, *2*, 1–61.
(63) Zapilko, C.; Liang, Y.; Anwander, R. *Chem. Mater.* **2007**, *19*, 3171–3176.
(64) Liang, Y.; Anwander, R. *Dalton Trans.* **2006**, 1909–1918.
(65) Huo, Q.; Leon, R.; Petroff, P. M.; Stucky, G. D. *Science* **1995**, *268*, 1324–1327.
(66) Huo, Q.; Margolese, D. I.; Stucky, G. D. *Chem. Mater.* **1996**, *8*, 1147–1160.
(67) Sakamoto, Y.; Kaneda, M.; Terasaki, O.; Zhao, D. Y.; Kim, J. M.; Stucky, G.; Shin, H. J.; Ryoo, R. *Nature* **2000**, *408*, 449–453.
(68) Kleitz, F.; Liu, D.; Anilkumar, G. M.; Park, I.-S.; Solovyov, L. A.; Shmakov, A. N.; Ryoo, R. *J. Phys. Chem. B* **2003**, *107*, 14296–14300.
(69) Polarz, S.; Kuschel, A. *Chem.—Eur. J.* **2008**, *14*, 9816–9829.
(70) Olmstead, M. M.; Power, P. P.; Shoner, S. C. *Inorg. Chem.* **1991**, *30*, 2547–2551.
(71) Chen, H.; Bartlett, R. A.; Dias, H. V. R.; Olmstead, M. M.; Power, P. P. *J. Am. Chem. Soc.* **1989**, *111*, 4338–4345.
(72) Duncan, J. S.; Nazif, T. M.; Verma, A. K.; Lee, S. C. *Inorg. Chem.* **2003**, *42*, 1211–1224.
(73) Gerstberger, G.; Palm, C.; Anwander, R. *Chem.—Eur. J.* **1999**, *5*, 997–1005.
(74) Kim, T.-W.; Ryoo, R.; Kruk, M.; Gierszal, K. P.; Jaroniec, M.; Kamiya, S.; Terasaki, O. *J. Phys. Chem. B* **2004**, *108*, 11480–11489.
(75) Zapilko, C.; Liang, Y.; Nerdal, W.; Anwander, R. *Chem.—Eur. J.* **2007**, *13*, 3169–3176.
(76) Kim, M. J.; Ryoo, R. *Chem. Mater.* **1999**, *11*, 487–491.
(77) Vinu, A.; Murugesan, V.; Hartmann, M. *Chem. Mater.* **2003**, *15*, 1385–1393.
(78) Zapilko, C.; Anwander, R. *Chem. Mater.* **2006**, *18*, 1479–1482.
(79) Deschner, T.; Liang, Y.; Anwander, R. *J. Phys. Chem. C* **2010**, *114*, 22603–22609.
(80) Deschner, T.; Lønstad, B.-T.; Widenmeyer, M.; Anwander, R. *J. Mater. Chem.* **2011**, *21*, 5620–5628.
(81) Anderson, M. W.; Egger, C. C.; Tiddy, G. J. T.; Casci, J. L.; Brakke, K. A. *Angew. Chem., Int. Ed.* **2005**, *44*, 3243–3248.
(82) Kruk, M.; Antochshuk, V.; Matos Jivaldo, R.; Mercuri Lucildes, P.; Jaroniec, M. *J. Am. Chem. Soc.* **2002**, *124*, 768–769.
(83) For the use of $Fe^{II}[N(SiMe_3)_2]_2$ and $Fe^{III}[N(SiMe_3)_2]_3$ for the synthesis of siloxane complexes, see: Nehete, U. N.; Anantharaman, G.; Chandrasekhar, V.; Murugavel, R.; Walawalkar, M. G.; Roesky, H. W.; Vidovic, D.; Magull, J.; Samwer, K.; Sass, B. *Angew. Chem., Int. Ed.* **2004**, *43*, 3832–3835.
(84) For the use of $Fe^{II}[N(SiMe_3)_2]_2$ for the synthesis of iron nanoparticles and -cubes, see: (a) Dumestre, F.; Chaudret, B.; Amiens, C.; Renaud, P.; Fejes, P. *Science* **2004**, *303*, 821–823. (b) Lacroix, L.-M.; Lachaize, S.; Falqui, A.; Respaud, M.; Chaudret, B. *J. Am. Chem. Soc.* **2009**, *131*, 549–557.
(85) For the use of $Fe^{II}[N(SiMe_3)_2]_2$ for the synthesis of Fe_xS_y clusters, see: (a) Ohki, Y.; Ikagawa, Y.; Tatsumi, K. *J. Am. Chem. Soc.* **2007**, *129*, 10457–10465. (b) Pyradun, R.; Holm, R. H. *Inorg. Chem.* **2008**, *47*, 3366–3370. (c) Ohki, Y.; Imada, M.; Murata, A.; Sunada, Y.; Ohta, S.; Honda, M.; Sasamori, T.; Tokitoh, N.; Katada, M.; Tatsumi, K. *J. Am. Chem. Soc.* **2009**, *131*, 13168–13178.
(86) For the use of $Fe^{II}[N(SiMe_3)_2]_2$ and its reactivity toward E−H-acidic substrates, see: Sulway, S. A.; Collison, D.; McDouall, J. J. W.; Tuna, F.; Layfield, R. A. *Inorg. Chem.* **2011**, *50*, 2521–2526 and references therein.
(87) Andersen, R. A.; Faegri, K., Jr.; Green, J. C.; Haaland, A.; Lappert, M. F.; Leung, W. P.; Rypdal, K. *Inorg. Chem.* **1988**, *27*, 1782–1786.
(88) Hursthouse, M. B.; Rodesiler, P. F. *J. Chem. Soc., Dalton Trans.* **1972**, 2100–2102.
(89) Siemeling, U.; Vorfeld, U.; Neumann, B.; Stammler, H.-G. *Inorg. Chem.* **2000**, *39*, 5159–5160.
(90) Edelmann, F. T.; Steiner, A.; Stalke, D.; Gilje, J. W.; Jagner, S.; Håkansson, M. *Polyhedron* **1994**, *13*, 539–546.
(91) Anwander, R.; Nagl, I.; Widenmeyer, M.; Engelhardt, G.; Groeger, O.; Palm, C.; Roeser, T. *J. Phys. Chem. B* **2000**, *104*, 3532–3544.
(92) Chen, J.; Li, Q.; Xu, R.; Xiao, F. *Angew. Chem., Int. Ed. Engl.* **1996**, *34*, 2694–2696.
(93) Ravikovitch, P. I.; Neimark, A. V. *Langmuir* **2002**, *18*, 1550–1560.
(94) (a) Eisch, J. J.; Adeosun, A. A.; Dutta, S.; Fregene, P. O. *Eur. J. Org. Chem.* **2005**, 2657–2670. (b) Fürstner, A.; Martin, R.; Krause, H.; Seidel, G.; Goddard, R.; Lehmann, C. W. *J. Am. Chem. Soc.* **2008**, *130*, 8773–8787.
(95) Goldfarb, D.; Bernard, M.; Strohmainer, K. G.; Vaughan, D. E. W.; Thomann, H. *J. Am. Chem. Soc.* **1994**, *116*, 6344–6353.
(96) Weckhuysen, B. M.; Wang, D.; Rosynek, M. P.; Lunsford, J. H. *Angew. Chem., Int. Ed. Engl.* **1997**, *36*, 2374–2376.
(97) Selvam, P.; Dapurkar, S. E.; Badamali, S. K.; Murugasam, M.; Kuwano, H. *Catal. Today* **2001**, *68*, 69–74.
(98) Carvalo, W. A.; Wallau, M.; Schuchardt, U. *J. Mol. Catal. A* **1999**, *144*, 91–99.
(99) Lin, D. H.; Coudurier, G.; Vedrine, J. C. *Stud. Surf. Sci. Catal.* **1989**, *49*, 1431–1448.
(100) Tuel, A.; Acron, I.; Miller, J. M. M. *J. Chem. Soc., Faraday Trans.* **1998**, *94*, 3501–3510.
(101) Bordiga, S.; Buzzoni, R.; Geobaldo, F.; Lamberti, C.; Giamello, E.; Zecchina, A.; Leofanti, G.; Petrini, G.; Tozzola, G.; Vlaic, G. *J. Catal.* **1996**, *158*, 486–501.
(102) Eppinger, J.; Herdtweck, E.; Anwander, R. *Polyhedron* **1998**, *17*, 1195–1201.
(103) Zapilko, C.; Widenmeyer, M.; Nagl, I.; Estler, F.; Anwander, R.; Raudaschl−Sieber, G.; Groeger, O.; Engelhardt, G. *J. Am. Chem. Soc.* **2006**, *128*, 16266–16276.
(104) Brunauer, S.; Emmett, P. H.; Teller, E. *J. Am. Chem. Soc.* **1938**, *60*, 309–319.
(105) Sing, K. S. W.; Everett, D. H.; Haul, R. A. W.; Moscou, L.; Pierotti, R. A.; Rouquerol, J.; Siemieniewska, T. *Pure Appl. Chem.* **1985**, *57*, 603–619.
(106) Barrett, E. P.; Joyner, L. G.; Halenda, P. P. *J. Am. Chem. Soc.* **1951**, *73*, 373–380.
(107) Sheldrick, G. M. *Acta Crystallogr.* **2008**, *A64*, 112–122.
(108) Farrugia, L. J. *J. Appl. Crystallogr.* **1997**, *30*, 565.